

# Integrating Superlattice to Regulate P2-O2 Phase Transition and Improve Cycling Stability in Sodium-Ion Batteries

Jiameng Feng,<sup>[a]</sup> Zhe Yang,<sup>[a]</sup> Jianjian Zhong,<sup>[a]</sup> Chaoliang Zheng,<sup>[a]</sup> Zhicheng Wei,<sup>[a]</sup> and Jianling Li<sup>\*[a]</sup>

P2-Na<sub>2/3</sub>Ni<sub>1/3</sub>Mn<sub>2/3</sub>O<sub>2</sub> is a promising cathode material for sodium-ion batteries (SIBs), but it faces the rapid capacity decay due to P2-O2 phase transition. The superlattice is a stable structure, compositing it can effectively eliminate the P2-O2 phase transition. Based on superlattice of NaLi<sub>1/3</sub>Mn<sub>2/3</sub>O<sub>2</sub>, a series of  $x\text{NaLi}_{1/3}\text{Mn}_{2/3}\text{O}_2 \cdot (1-x)\text{Na}_{2/3}\text{Ni}_{1/3}\text{Mn}_{2/3}\text{O}_2$  ( $x=0, 0.3, 0.4, 0.5$ ) were first synthesized by compounding NaLi<sub>1/3</sub>Mn<sub>2/3</sub>O<sub>2</sub> into Na<sub>2/3</sub>Ni<sub>1/3</sub>Mn<sub>2/3</sub>O<sub>2</sub> in this article. The XRD and SAED show that special superlattice guarantees the structure stable of materials,

resulting in a first order phase transformation to a solid solution reaction in high voltage. The composite cathode materials realize excellent cycle performance and discharge specific capacity. When  $x=0.4$ , the capacity retention rate is 82.64% after 100 cycles, which is greatly improved compared with 30.60% of Na<sub>2/3</sub>Ni<sub>1/3</sub>Mn<sub>2/3</sub>O<sub>2</sub>. This paper provides a new idea for using superlattice to stabilize the structure and improve the electrochemical performance for SIBs.

## Introduction

Energy is the driving force and source of production. With the increasing demand for energy and the depletion of natural resources, people need to strictly control the consumption of fossil fuels and find new energy.<sup>[1]</sup> At present, new energy sources mainly include solar energy,<sup>[2]</sup> wind energy,<sup>[3]</sup> geothermal energy<sup>[4]</sup> and tidal energy,<sup>[5]</sup> etc. However, the output of their energy is intermittent and territorial in nature.<sup>[6]</sup> In order to effectively utilize such energy sources, energy storage systems need to be established first.<sup>[7]</sup> Lithium-ion batteries (LIBs) are now successfully used in various portable electronic devices and other energy storage devices.<sup>[8]</sup> However, the finite resource reserves and increased costs severely limit the widespread use of LIBs.<sup>[9]</sup> In this backdrop, based on the richness and wide distribution of global sodium resources, the sodium-ion batteries (SIBs) begin to attract attention in the field of large-scale energy storage.<sup>[10]</sup>

The cathode material is one of the most important components of the battery. SIBs cathode materials are mainly divided into transition metal layered oxides,<sup>[11]</sup> polyanionic compounds,<sup>[12]</sup> Prussian blue type<sup>[13]</sup> and organic material type.<sup>[14]</sup> Among them, transition metal layered oxides have attracted much attention because of their low cost, simple synthesis process and high electrochemical activity.<sup>[15]</sup> Nevertheless, layered oxides also face a series of problems such as instability in air, irreversible phase transition in the high-voltage

region, Na<sup>+</sup>/vacancies ordering during cycling.<sup>[16]</sup> In the research and development of electrode materials for secondary batteries, the study of composite materials is an important part of the discovery of new materials. Because the composite materials can play a synergistic effect between each component, the performance of the material can reach the best use conditions.<sup>[17]</sup> Feng's group<sup>[18]</sup> introduced Li<sub>2</sub>MnO<sub>3</sub> into NaNi<sub>1/3</sub>Co<sub>1/3</sub>Mn<sub>1/3</sub>O<sub>2</sub>. The X-ray diffraction (XRD) showed that P2-type structure easily formed with the increase of Li<sub>2</sub>MnO<sub>3</sub>, and the Li<sub>2</sub>MnO<sub>3</sub> in the composites greatly improved the reversible specific capacity and interfacial stability under high cut-off voltage operation (4.8 V). A novel composite structure  $x\text{Na}_4\text{Mn}_2\text{O}_5 \cdot (1-x)\text{Na}_{0.7}\text{MnO}_2$  was designed and synthesized by Liu,<sup>[19]</sup> and their sodium storage performance were systematically investigated. The results indicated that the optimized 0.44Na<sub>4</sub>Mn<sub>2</sub>O<sub>5</sub>·0.56Na<sub>0.7</sub>MnO<sub>2</sub> exhibited a considerable initial discharge capacity of 228.0 mAh g<sup>-1</sup>, a stable crystal structure and high reversible ability in the deoxygenation/adsorption process.

The electrochemical properties of Na<sub>2/3</sub>Ni<sub>1/3</sub>Mn<sub>2/3</sub>O<sub>2</sub> were reported by Dahn in 2001.<sup>[20]</sup> On the basis of the redox of Ni, Na<sub>2/3</sub>Ni<sub>1/3</sub>Mn<sub>2/3</sub>O<sub>2</sub> is able to achieve a reversible specific capacity of 150 mAh g<sup>-1</sup> in the voltage range of 2.0–4.5 V. But there is a P2-O2 phase transition around 4.2 V, which leads to a rapid decay of specific capacity. The layered Li<sub>2</sub>MnO<sub>3</sub> can be expressed as Li[Li<sub>1/3</sub>Mn<sub>2/3</sub>]O<sub>2</sub> with the space group C2/m. Based on Li[Li<sub>1/3</sub>Mn<sub>2/3</sub>]O<sub>2</sub>, we synthesized Na[Li<sub>1/3</sub>Mn<sub>2/3</sub>]O<sub>2</sub>, a cathode material for SIBs, which has similar superlattice structure and electrochemical properties to Li[Li<sub>1/3</sub>Mn<sub>2/3</sub>]O<sub>2</sub>. In the transition metal (TM) layer of Na[Li<sub>1/3</sub>Mn<sub>2/3</sub>]O<sub>2</sub>, lithium, oxygen and TM are stacked one after another in ABCABC stacking order (Figure 1a). That means 1/3 of Mn<sup>4+</sup> in the TM layer is replaced by Li<sup>+</sup>. Due to this occupation of Li<sup>+</sup> in the TM layer, there exists a honeycomb structure consisting of six Mn<sup>4+</sup> around one Li<sup>+</sup> (Figure 1b), and this structure is the superlattice structure,

[a] J. Feng, Z. Yang, J. Zhong, C. Zheng, Z. Wei, Prof. J. Li  
State Key Laboratory of Advanced Metallurgy,  
School of Metallurgical and Ecological Engineering  
University of Science and Technology Beijing  
Beijing 100083, China  
E-mail: lijianling@ustb.edu.cn

 Supporting information for this article is available on the WWW under  
<https://doi.org/10.1002/batt.202200115>

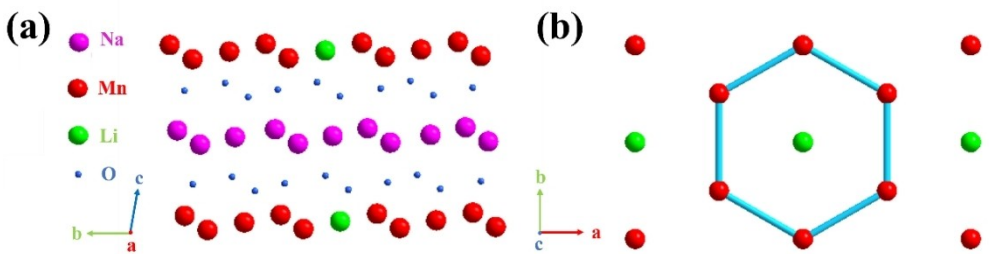


Figure 1. The crystal structure of  $\text{NaLi}_{1/3}\text{Mn}_{2/3}\text{O}_2$ .

which can greatly improve the cyclic stability of the material.<sup>[21]</sup> During the charging process, sodium ions are removed from the layer structure, which leads to an increase in the repulsive force between O–O, thus allowing irreversible slip of the TM layer. The superlattice acts as a peg to keep Mn in the TM layer when charging, thus inhibiting the slip of the TM layer and the dissolution of manganese. In this paper, we successfully introduce the superlattice of  $\text{NaLi}_{1/3}\text{Mn}_{2/3}\text{O}_2$  into  $\text{Na}_{2/3}\text{Ni}_{1/3}\text{Mn}_{2/3}\text{O}_2$ . The experiments show that the introduction of  $\text{NaLi}_{1/3}\text{Mn}_{2/3}\text{O}_2$  not only improves the structural stability of the composite cathode materials under high voltage, but also enhances the

sodium ion kinetic performance and obtains better cycling performance.

## Results and discussion

As shown in Figure 2(a), all composite cathode materials  $x\text{NaLi}_{1/3}\text{Mn}_{2/3}\text{O}_2 \cdot (1-x)\text{Na}_{2/3}\text{Ni}_{1/3}\text{Mn}_{2/3}\text{O}_2$  ( $x=0, 0.3, 0.4, 0.5$ ) are indexed to a P2-type structure with the space group P63/mmc, and are marked as X0, X0.3, X0.4, X0.5 according to the value of  $x$  for convenient. Rietveld refinement is performed based on P63/mmc to further confirm the results as shown in Figure 2(b–d).

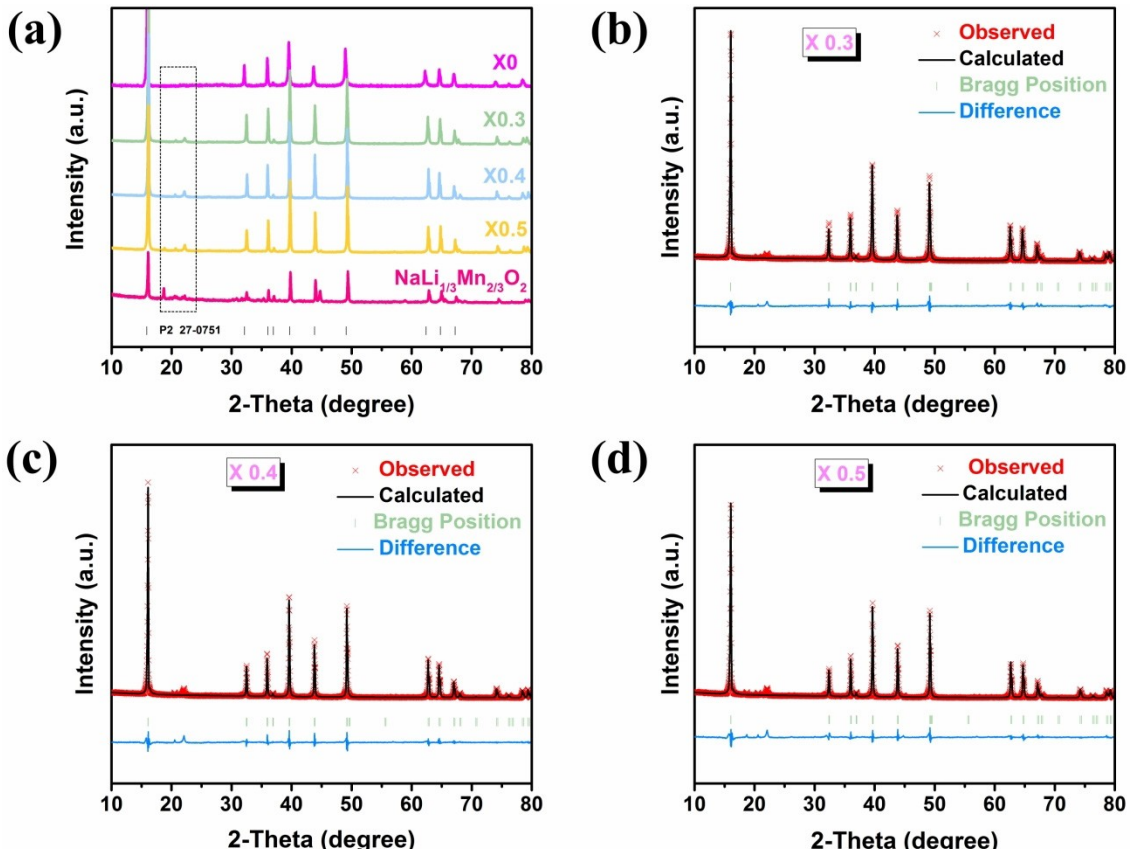


Figure 2. a) The XRD patterns of the composite cathode materials; Rietveld refinement patterns for the b) X0.3; c) X0.4; d) X0.5.

d). The detailed Rietveld refinement data are shown in Table S1. Accordingly, the sodium ions are located in the trigonal structure. The diffraction peaks of all composite cathode materials can be considered as a combined structure of  $\text{NaLi}_{1/3}\text{Mn}_{2/3}\text{O}_2$  and  $\text{Na}_{2/3}\text{Ni}_{1/3}\text{Mn}_{2/3}\text{O}_2$ , and all of which are sharp and exhibit good crystallinity. With the increase of  $x$ , the diffraction peak of  $\text{NaLi}_{1/3}\text{Mn}_{2/3}\text{O}_2$  component becomes more obvious. When  $x=0.5$ , a new diffraction peak appears at  $18.8^\circ$ , which is the diffraction peak of  $\text{NaLi}_{1/3}\text{Mn}_{2/3}\text{O}_2$ . The intensity evolution of the new peak indicates a subtle change in the crystal structure of the composite cathode materials. And the diffraction peaks located at  $20^\circ$  and  $22^\circ$  proof the ordered arrangement of Li and Mn in the transition metal layer. In addition, the superlattice of the ordered arrangement of Li and Mn in the transition metal layer can also be seen in the selected area electron diffraction (SAED) below.

The morphology of the composite cathode materials is characterized by the scanning electron microscopy (SEM). As can be seen in Figure 3(b), the morphology of the composite cathode material is similar to a platform with a flat and regular surface. The crystallinity is good, and the particle size is about  $1\text{--}2\ \mu\text{m}$  with a slight difference. Compared to  $\text{Na}_{2/3}\text{Ni}_{1/3}\text{Mn}_{2/3}\text{O}_2$  in Figure 3(a), the particles of the X0.4 are slightly smaller and more uniform in size, indicating shorter sodium ion transport channels and easier electron transport. The energy dispersive X-ray spectroscopy (EDS) mapping demonstrates that the individual elements of Na, Ni, Mn, and O are distributed uniformly in the composite in the Figure 3(c-g).

To explore the effect on the electrochemical performance of the composite cathode materials after compounding  $\text{NaLi}_{1/3}\text{Mn}_{2/3}\text{O}_2$ , the electrochemical performance of the composite cathode materials is tested in a half-cell with a voltage range of  $2.0\text{--}4.5\ \text{V}$  ( $1\ \text{C}=173\ \text{mAh g}^{-1}$ ). Figure 4(a) reveals a typical charge/discharge curve of the composite cathode materials for the first cycle at  $0.05\ \text{C}$ . From the Figure S1, the reversible capacity of pure  $\text{NaLi}_{1/3}\text{Mn}_{2/3}\text{O}_2$  is only  $80\ \text{mAh g}^{-1}$ , while the composite cathode material X0.4 exhibits a reversible specific capacity of  $150\ \text{mAh g}^{-1}$  with a smaller polarization. The first cycle charging curve of  $\text{Na}_{2/3}\text{Ni}_{1/3}\text{Mn}_{2/3}\text{O}_2$  shows a long plateau

at  $4.2\ \text{V}$ , which corresponds to the P2-O2 phase transition, while the charging and discharging curve of the composite cathode materials are a completely inclined sloping line, indicating that the P2-O2 phase transition at  $4.2\ \text{V}$  is completely suppressed. When charged to about  $4.5\ \text{V}$ , the long plateau in the charge-discharge curve corresponds to the anion redox reaction, which is further confirmed in the cyclic voltammetry (CV) curve. As shown in Figure 4(c), fewer peaks appear in the CV curves of the composite cathode material X0.4, which corresponds to a smoother charge/discharge curve. This demonstrates that the superlattice structure suppresses the  $\text{Na}^+/\text{vacancy}$  ordering below  $4.0\ \text{V}$  and the P2-O2 phase transition at  $4.2\ \text{V}$  of  $\text{Na}_{2/3}\text{Ni}_{1/3}\text{Mn}_{2/3}\text{O}_2$ . Therefore, the composite cathode materials maintain a more stable structure during the sodium ion de-embedding process.

As displayed in Figure 4(b), the composite cathode materials exhibit excellent multiplicative performance at different current densities. When  $x=0.4$ , the rate performance is at its best, and the high discharge specific capacity can be maintained at different current densities of  $0.05\text{C}$ ,  $0.1\text{C}$ ,  $0.2\text{C}$ ,  $0.3\text{C}$ ,  $0.5\text{C}$ ,  $1\text{C}$ ,  $2\text{C}$  and  $5\text{C}$ . In addition, it is able to return to the initial discharge specific capacity when it returns to  $0.05\text{C}$  again, which indicates that the composite cathode materials can keep the structural stability and capacity reversibility even after charging and discharging at high current density. The improved rate performance at high current densities may be due to the fact that  $\text{NaLi}_{1/3}\text{Mn}_{2/3}\text{O}_2$  in the composite cathode materials counteracts the slippage of the transition metal layer caused by sodium ion de-embedding during cycling, and the complete solid-solution reaction results in greatly enhanced sodium ion kinetics. Figure 4(d) shows the cycling performance of the composite cathode materials. The capacity retention rates of X0, X0.3, X0.4 and X0.5 after 100 cycles at  $0.5\ \text{C}$  are  $30.6\%$ ,  $65.1\%$ ,  $82.6\%$  and  $64.1\%$ , respectively. The reason for this disparity may be that different degrees of  $\text{Na}^+/\text{vacancy}$  ordering play a role in the cycling process, which remains to be further investigated. And the Coulombic efficiency (CE) of the composite material (98.5%) is also higher than X0 (94.6%) in the long cycling. However, the CE of the composite material is

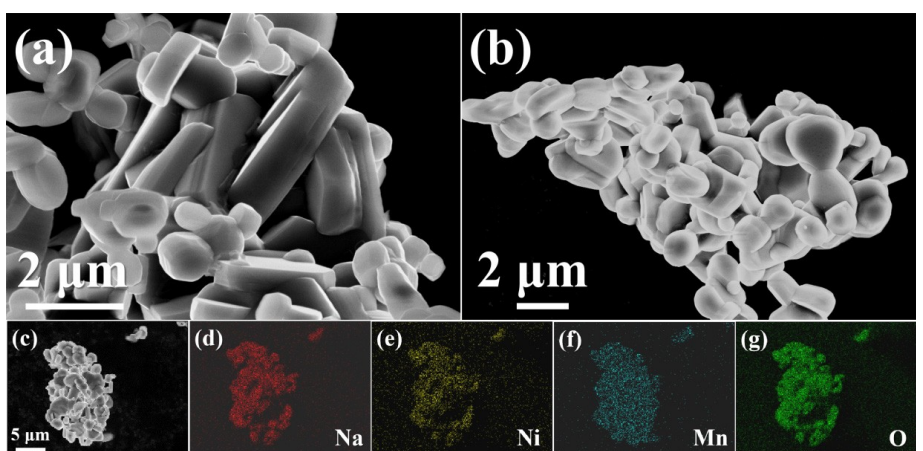
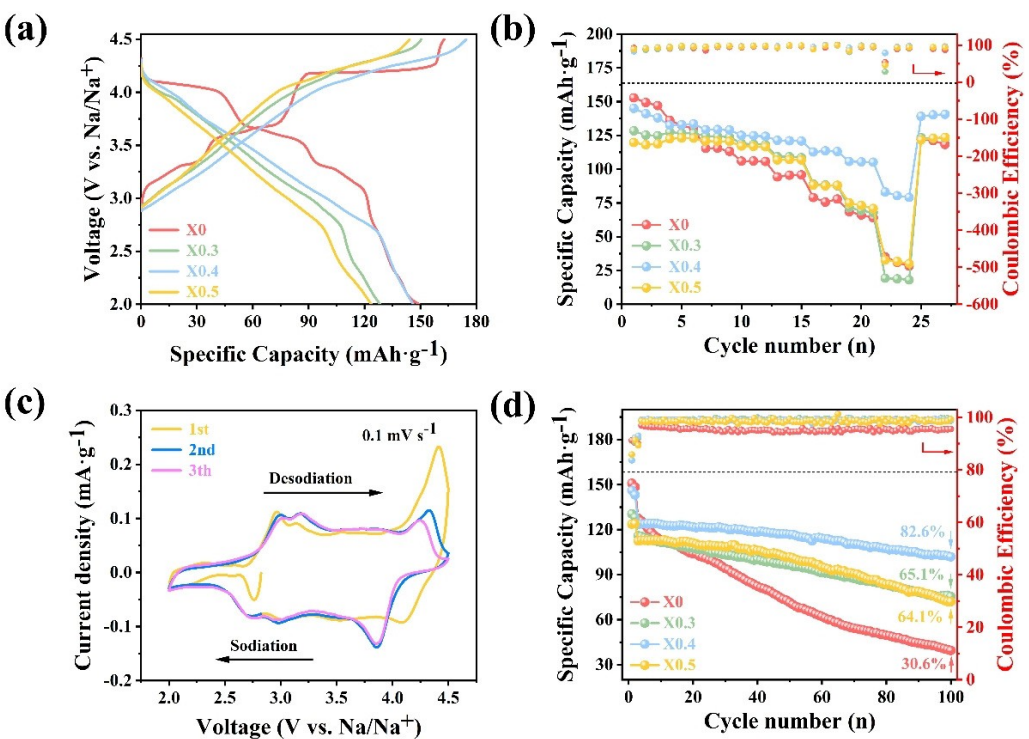


Figure 3. SEM image of a) X0; b) X0.4; c–g) EDS mapping images of X0.4.



**Figure 4.** a) The charge-discharge curves in the voltage range of 2.0–4.5 V; b) rate performance of composite cathode materials at different rates; c) CV of X0.4; d) cycling performance of composite cathode materials at 0.5 C.

low in the first cycle. According to the relevant literature,<sup>[22]</sup> it may be caused by the formation of dendrites during the cycling. To reduce the dendrites, the appropriate additives, such as the Fluoroethylene carbonate (FEC), can be added to the electrolyte or increase the activation current density in the first few cycles. All of these lead to a reduction in dendrites and an increase in CE. Compounding NaLi<sub>1/3</sub>Mn<sub>2/3</sub>O<sub>2</sub> into Na<sub>2/3</sub>Ni<sub>1/3</sub>Mn<sub>2/3</sub>O<sub>2</sub>, the superlattice with ordered arrangement of Li/Mn stabilizes the crystal structure during the cycling process. Moreover, the sodium content of the composite cathode materials is increased so that more sodium ions can remain in the alkali metal layer during the discharge process. Higher sodium content in the alkali metal layer in the charging high voltage region can likewise eliminate the P2-O2 phase transition, thus improving the structural stability and capacity retention during cycling.

As shown in Figure 5(a), to further understand the structural evolution of the composite cathode materials during sodium ion extraction and insertion, ex-situ XRD tests are performed on X0.4 at different charge and discharge states between 2.0 and 4.5 V during the first cycle. During the charging process, the diffraction peaks of (100), (102), and (103) crystal planes shift to a high angle with the detachment of Na<sup>+</sup>, which indicates the narrowing of the ab plane. At the same time, the diffraction peaks of (002) and (004) crystal planes shift to a lower angle, which indicates that the c-axis becomes longer. This is caused by the fact that when sodium ions are taken off, the electrostatic repulsion between oxygen atoms becomes larger thus leading to an increase in the distance between adjacent oxygen

layers. The variation of cell parameters is further analyzed by Rietveld refinement and the results are shown in Figure S2(a-f). Figure S3 and Table S2 show the variation of *a*-axis and *c*-axis in different charging and discharging states by Rietveld refinement. At the end of charging, no new peak is generated, which indicates that no P2-O2 phase transition or P2-OP4 phase transition occurs at 4.5 V. However, all the peaks broaden at 4.5 V, which indicates that the crystallinity of the composite cathode material deteriorates at the end of charging. But the diffraction peak width gradually recovers as the discharge proceeds. During the discharge process, the sodium ions are embedded in the alkali metal layer and all the diffraction peaks return to their initial positions, which indicates that the composite cathode materials are highly reversible and conducive to structural stability for long-term cycling. No new peak appears during the whole charging and discharging process, which means that the composite cathode materials undergo a complete solid-solution reaction without any phase transition during the sodium ion de-embedding process.<sup>[23]</sup> It is worth emphasizing that the superlattice peak between 20°–25° can be seen in Figure 5(b) accompanying the whole charging and discharging process. From the SEM (Figure S4) of the pristine state and the end of the first cycle (charge to 4.5 V then discharge to 2.0 V), there are no morphological changes, no surface cracks, and no alteration of particle size of the composite cathode material X0.4 after the cycle. It indicates that a collapse of the material structure does not occur during the charging and discharging process.

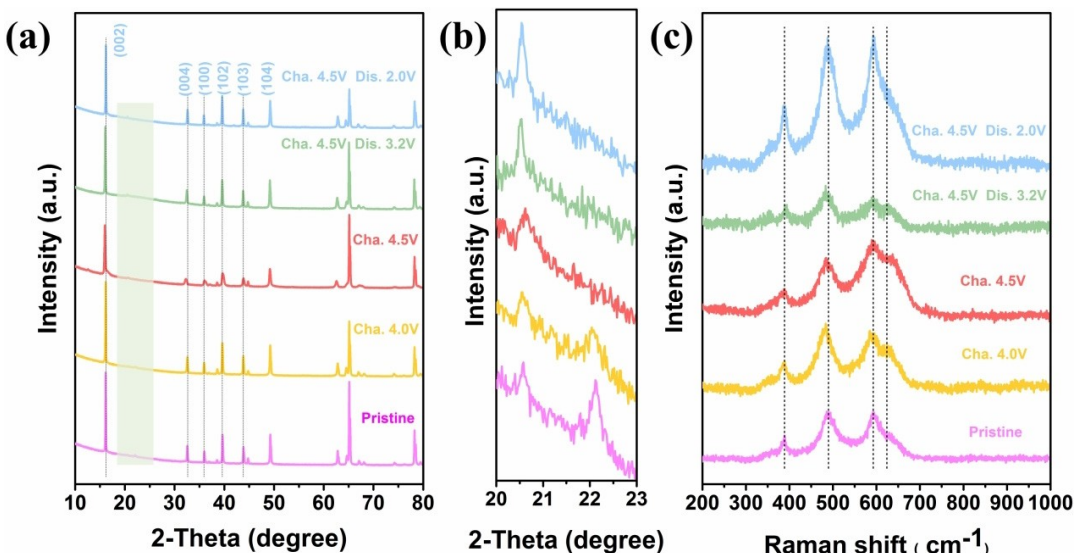


Figure 5. a) XRD diffraction of X0.4 in different states; b) local magnification of (a); c) Raman spectroscopy of X0.4 in different states.

Raman spectra is used to study the changes of the short-range structure of the composite cathode materials during charging and discharging. Figure 5(c) compares the Raman spectra of the X0.4 under different charging and discharging states. Three distinct scattering peaks exist at 388, 487, and 592 cm<sup>-1</sup>, which gradually become weaker during the charging process and then gradually increase during the discharging process. In addition, the peak at 625 cm<sup>-1</sup> belongs to the characteristic peak of Na<sup>+</sup>/vacancy that appears during charging and fades away during discharging.<sup>[24]</sup> The band around 384 cm<sup>-1</sup> is similar to the characteristic band of NaLi<sub>1/3</sub>Mn<sub>2/3</sub>O<sub>2</sub>

with a [Li<sub>1/3</sub>Mn<sub>2/3</sub>] superlattice structure, which remains after the end of the discharge.<sup>[25]</sup> Hence, it can be presumed that the superlattice structure is maintained during the electrochemical process.

In order to explore the charge compensation mechanism during sodium ion extraction/insertion, we use the X-ray photoelectron spectroscopy (XPS) to study the valence changes of active ions in the electrode under different charging and discharging states. Here, the software CasaXPS is applied for peak fitting. As shown in Figure 6(a), the binding energy of Mn2p are around 642.2 eV and 653.9 eV, respectively. During

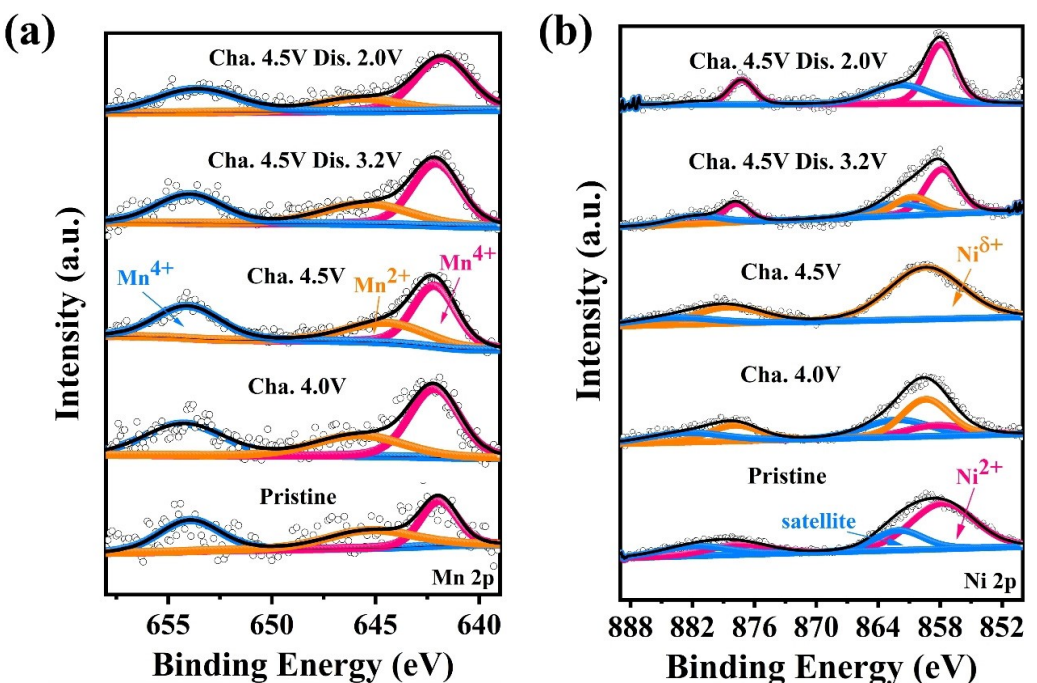
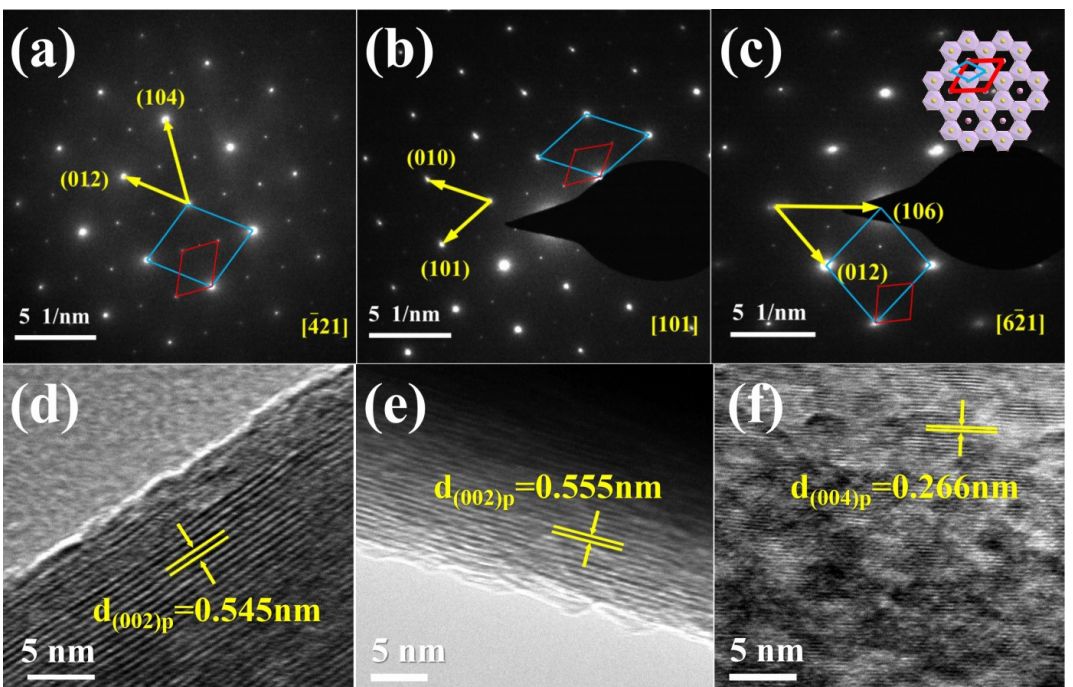


Figure 6. XPS spectra of the X0.4 in different states of charge and discharge: a) Mn 2p; b) Ni 2p.

the charging process, the valence state of Mn does not change much, even when discharged to 3.2 V, Mn still does not change valence significantly. But when discharged deeply, the peak of Mn shifts to the low binding energy, which indicates that a little part of Mn changes to the low valence state due to the reduction reaction when discharged to 2 V. This indicates that Mn plays a role in stabilizing the structure of the material. In Figure 6(b), the Ni2p spectra in either charge/discharge state of the electrode sheet show both  $\text{Ni}2\text{p}_{3/2}$  and  $\text{Ni}2\text{p}_{1/2}$  as well as their satellite peaks. Nickel exhibits electrochemical activity in the charge and discharge process. During the charging process,  $\text{Ni}^{2+}$  gradually decreases and  $\text{Ni}^{\delta+}$  (represent the oxidation state of nickel) gradually increases, and almost all  $\text{Ni}^{2+}$  is oxidized to higher valence states when charged to 4.5 V. During the discharge process, Ni undergoes a reduction reaction, and the oxidized state of Ni gradually returns to  $\text{Ni}^{2+}$ . It is marked that the charge compensation is carried out mainly by the redox reaction of Ni, especially at low voltages during the embedding and detachment of sodium ions. The high sodium content in the structure of the P2 phase not only enhances the stability of the matrix structure, but also promotes the oxidation of low-valent cations to their high-oxidation states to a certain extent. The main reason is that the high sodium content can affect the hybridization state between O2p and TM (3d-eg) orbitals in the layered oxide, prompting the material to achieve a multi-electron redox reaction from  $\text{Ni}^{2+}$  to  $\text{Ni}^{4+}$  in the voltage range of 4.0 V. The high sodium content also can affect the local environment of transition metals in the structure and the interaction between  $\text{NaO}_2$  and  $\text{TMO}_2$  layers, eliminating the structural transition from the P2 phase to the O2 phase of the structure.

The crystal structure of the material is further investigated by the selected area electron diffraction (SAED) and the high-resolution transmission electron microscopy (HRTEM), as shown in Figure 7. SAED of the composite cathode material shows a structure with alternating rows of bright spots and dark spots, as indicated by blue and red frames in Figure 7(a–c). The bright spots are typical electron diffraction pattern of conventional layered materials, while the dark spots are unique to this material and arise due to the superlattice by  $[\text{Li}_{1/3}\text{Mn}_{2/3}]$  units in the composite cathode material. And they still present when charged to 4.5 V and discharged to 2.0 V, which means that the superlattice is well retained during charge and discharge. In Figure 7(d–f), the planar spacing between adjacent lattice stripes is found to be approximately 0.545 nm, corresponding to the spacing of  $d$  with (002) peak in the P2 phase structure. Furthermore, the planar spacing increases slightly when charged to 4.5 V, which is consistent with the results in ex-situ XRD.

The formation and growth of intergranular cracks usually occur in laminated materials during cycling, which is detrimental to the charge transfer between and within the particles, thus limiting the rate capability and cycling performance. In addition, it is not negligible that the decomposition of the electrolyte is catalyzed at the electrode/electrolyte interface. The deterioration of the solid/electrolyte interface interaction due to increased contact area between the electrode surface and electrolyte. Further, it may lead to poor cycling performance caused by increased cracking. The cell of X0.4 after 50 cycles is disassembled and the electrode sheet is taken out for SEM and XRD tests. As shown in Figure 8, the X0.4 still maintains the P2 phase after 50 cycles, and the superlattice



**Figure 7.** SAED images of X0.4 in different states: a) the pristine; b) charge to 4.5 V; c) charge to 4.5 V then discharge to 2.0 V; HRTEM images of X0.4 in different states: d) The pristine; e) Charge to 4.5 V; f) Charge to 4.5 V then discharge to 2.0 V.

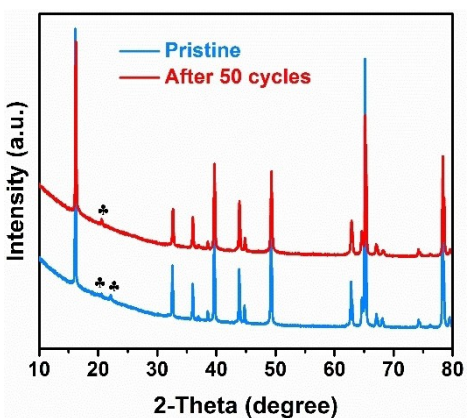


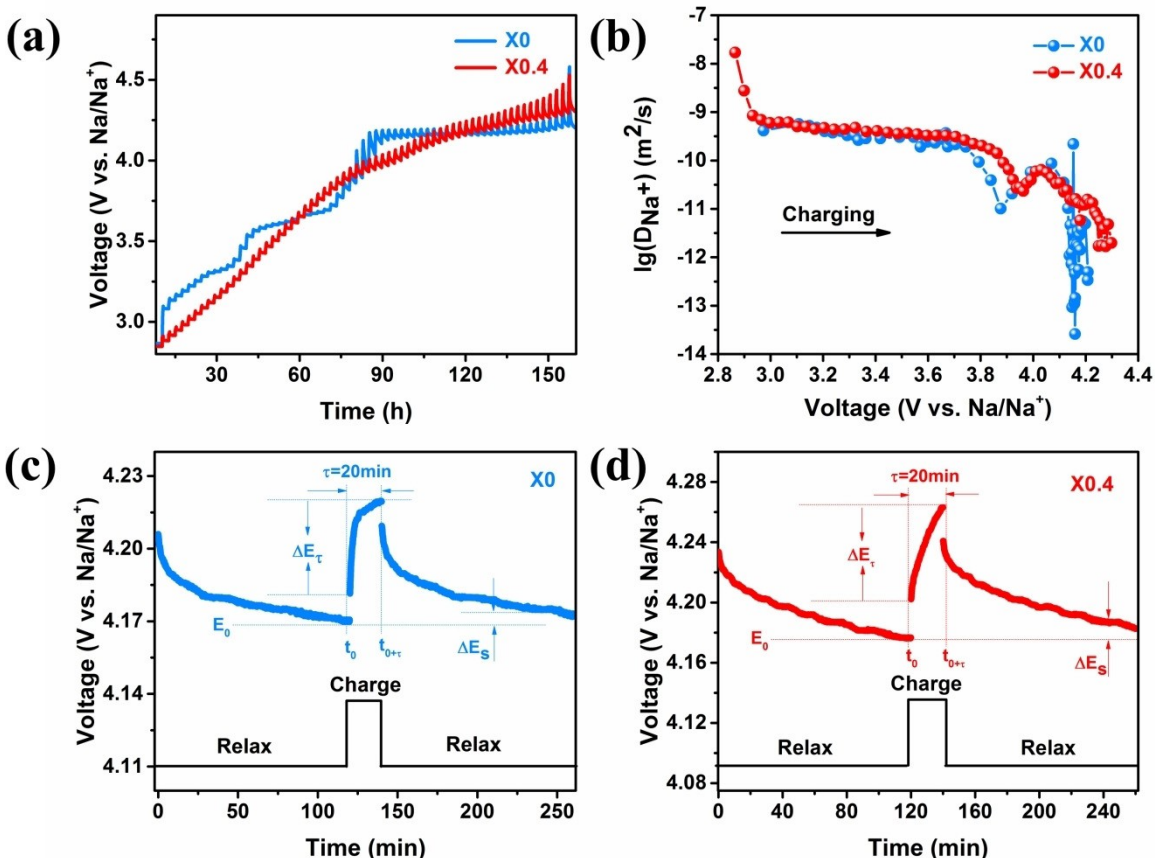
Figure 8. XRD before and after 50 cycles of X0.4.

structure also exists. This indicates that a single-phase solid-solution reaction occurs during cycling with superlattice stability, which corresponds to an excellent cycling stability. It can be seen from Figure S5, there is no obvious crack in the cathode material after 50 cycles of X0.4, which can also prove the stability of the crystal structure. In Figure S5b, it can be found that a stable CEI film is formed on the surface of the cathode material after 50 cycles, which protects the cathode material from erosion by the electrolyte during the cycles.

The sodium ion diffusion coefficient ( $D_{Na^+}$ ) of X0.4 is studied using the galvanostatic intermittent titration test (GITT), as shown in Figure 9. In this experiment, an electrostatic current pulse of 0.05 C is applied for 20 min, followed by a relaxation of 120 min. Figure 9(a) shows the typical GITT curves of the X0 and X0.4 electrodes in a voltage window of 2.0–4.5 V. Figure 9(b) shows the  $D_{Na^+}$  during the first charge. Figure 9c and Figure 9d show a complete test single section of an arbitrarily selected segment of the charging curve. The  $D_{Na^+}$  can be obtained from the following equation:

$$\tilde{D}_{Na} = \frac{4}{\pi \tau} \left( \frac{m_B V_m}{M_B S} \right)^2 \left( \frac{\Delta E_s}{\Delta E_t} \right)^2 \left( \tau \leq L^2 / \tilde{D}_{Na} \right) \quad (1)$$

where  $m_B$ ,  $M_B$ ,  $V_m$ , and  $S$  denote the mass, atomic weight, molar volume, and surface area of the electrode material, respectively.  $\Delta E_s$  is the variation of the balance voltage and  $\Delta E_t$  is the change in the instantaneous voltage during the pulse time. Figure S6 shows a linear relationship between  $E$  and  $\tau^{1/2}$ , demonstrating the feasibility of using the GITT to study the sodium ion diffusion kinetics. From Figure 9(b), the  $D_{Na^+}$  of X0.4 ranges from  $8.96 \times 10^{-11} \text{ cm}^2 \text{s}^{-1}$  to  $8.46 \times 10^{-10} \text{ cm}^2 \text{s}^{-1}$  in the voltage range 2.9–3.9 V, while the sodium ion diffusion coefficient of X0 ranges from  $1.01 \times 10^{-11} \text{ cm}^2 \text{s}^{-1}$  to  $5.66 \times 10^{-10} \text{ cm}^2 \text{s}^{-1}$ . Compared with X0, X0.4 shows a larger sodium ion migration rate and more stable structure. When the voltage

Figure 9. a) The GITT curves of material in the voltage range of 2.0–4.5 V; b) the  $D_{Na^+}$  of material; schematic diagram of GITT of c) X0; d) X0.4.

reaches higher than 4.0 V, the sodium ion diffusion coefficient decreases sharply. The  $D_{\text{Na}^+}$  of X0.4 reaches a minimum value of  $1.68 \times 10^{-12} \text{ cm}^2 \text{s}^{-1}$  at around 4.3 V; while the  $D_{\text{Na}^+}$  of X0 drops sharply to  $2.60 \times 10^{-14} \text{ cm}^2 \text{s}^{-1}$  at around 4.2 V. During the first charge, the value of  $D_{\text{Na}^+}$  remained stable until the voltage reached 4.0 V, but the  $D_{\text{Na}^+}$  suddenly decreased above 4.0 V. This is mainly due to the deterioration of the material structure caused by the slip of the transition metal layer in the high voltage region, thus hindering the diffusion and migration of sodium ions.

Electrochemical impedance spectroscopy (EIS) is used to study the impedance of the composite cathode materials in the charging state (charged to 4.0 V) during electrochemical cycling. The electrode process is controlled by both charge transfer and diffusion processes, and the Nyquist plot is composed of a semicircle in the high frequency region and a straight line at  $45^\circ$  to the transverse axis in the low frequency region. The high frequency region is controlled by the charge transfer process in the electrode reaction kinetics, and the low frequency region is controlled by the diffusion of reactants or products of the electrode reaction. The intercept of the high frequency region with the real axis  $Z'$  is the ohmic impedance  $R_s$  inside the cell. The semicircle in the medium-high frequency region represents the impedance  $R_{sf}$  generated by the diffusion of  $\text{Na}^+$  by the SEI film produced on the electrode surface. The semicircle in the medium-low frequency region represents the charge transfer impedance  $R_{ct}$ . The diagonal line in the low frequency region represents the diffusion impedance of  $\text{Na}^+$  inside the material.

As shown in Figure 10(a and b), the resistance of X0 and X0.4 cells shows an increasing trend as the number of cycles increases. In the first cycle, the EIS profile of the material consists of only one semicircle in the high frequency region and a diagonal line in the low frequency region, while a semicircle appears in the high frequency region after 50 cycles. The equivalent circuit is shown in the illustration (in the Figure 10), and the  $R_{sf}$  and  $R_{ct}$  fitted by ZSimpWin software are summarized in the Table S3. It is found that the charge transfer impedance  $R_{ct}$  of X0.4 is significantly lower than that of X0, which indicates that the kinetic performance of X0.4 is better at the beginning of the cycle. The decrease in impedance is an

important reason for the good rate performance of the material, corroborating the above comparison between X0 and X0.4 of rate performance. After 50 cycles, the  $R_{ct}$  of sample X0.4 increases 89.4  $\Omega$ , while the  $R_{ct}$  of sample X0 increases 247.9  $\Omega$ . This suggests that the sample X0.4 undergoes less phase transition during the cycle and maintains better initial structure. Meanwhile, the  $R_{sf}$  of X0.4 is also much smaller than that of X0, manifesting that X0.4 has somewhat fewer side reactions with the electrolyte and effectively inhibits the formation of SEI film in a way. Moreover, when the TM layer slips during cycling, the TM ions dissolve in the electrolyte, which also leads to an increase in impedance.

In addition, the  $D_{\text{Na}^+}$  are calculated according to the following formula:<sup>[26]</sup>

$$D = \frac{1}{2} \left( \frac{RT}{An^2 F^2 C \sigma} \right)^2 \quad (2)$$

where  $R$  is the gas constant,  $T$  is the absolute temperature of the test environment,  $A$  is the area of the electrode,  $n$  is the number of electrons transferred per molecule,  $F$  is the Faraday constant,  $C$  is the bulk concentration of carrier-ion, and  $\sigma$  is the Warburg coefficient<sup>[27]</sup> (Figure 10, inset). It is calculated that the  $D_{\text{Na}^+}$  of X0.4 is  $1.93 \times 10^{-10} \text{ cm}^2 \text{s}^{-1}$ , which is higher than X0 with  $2.19 \times 10^{-11} \text{ cm}^2 \text{s}^{-1}$  after 1 cycle. Likewise, the  $D_{\text{Na}^+}$  of X0.4 is  $1.20 \times 10^{-10} \text{ cm}^2 \text{s}^{-1}$ , which is also higher than X0 with  $2.78 \times 10^{-12} \text{ cm}^2 \text{s}^{-1}$  after 50 cycles. Unsurprisingly, the above results are almost consistent with the  $D_{\text{Na}^+}$  obtained from GITT, further demonstrating the reliability of the GITT data and the improved dynamic performance of the composite material.

## Conclusion

In this paper, the composite cathode material  $x\text{NaLi}_{1/3}\text{Mn}_{2/3}\text{O}_2 \cdot (1-x)\text{Na}_{2/3}\text{Ni}_{1/3}\text{Mn}_{2/3}\text{O}_2$  ( $x=0, 0.3, 0.4, 0.5$ ) for sodium-ion battery is successfully designed and prepared. The structural stability of the composite cathode materials is improved by introducing  $\text{NaLi}_{1/3}\text{Mn}_{2/3}\text{O}_2$  into  $\text{Na}_{2/3}\text{Ni}_{1/3}\text{Mn}_{2/3}\text{O}_2$ . The sample X0.4 with sufficient sodium content has a discharge specific capacity of  $150 \text{ mAh g}^{-1}$  in the voltage range of 2.0–4.5 V, with

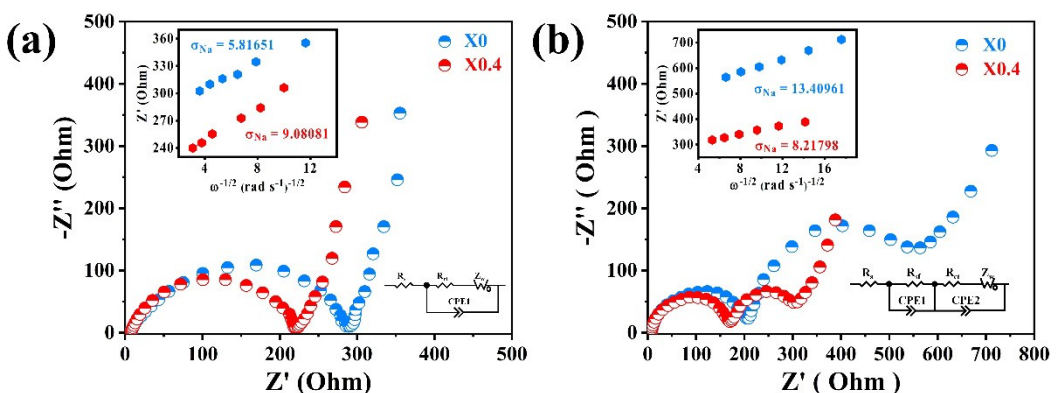


Figure 10. EIS test of X0 and X0.4 at different number of cycles: a) 1st cycle; b) After 50 cycles.

good rate performance of  $72.48 \text{ mAh g}^{-1}$  at 5 C and outstanding capacity retention of 82.6% after 100 cycles at 0.5 C. Owing to the superlattice consisting of the ordered arrangement Li and Mn in the transition metal layer, the crystal structure of the composite material is more stable when sodium ions are removed, which eliminates the P2-O2 phase transition during charging and discharging. Even after 50 cycles, the superlattice is still maintained, which results in smaller volume change contributing to the reduction of surface cracks. Due to the reduced grain size and the complete solid solution reaction during the charging and discharging process, the sodium-ion kinetics in the composite cathode material is significantly enhanced, especially in the high voltage region. Finally, the research work reveals the key role of the superlattice in maintaining structural stability, presenting a new method for synthesizing stable cycling sodium-ion batteries.

## Experimental Section

### Material synthesis

The composite cathode materials  $x\text{NaLi}_{1/3}\text{Mn}_{2/3}\text{O}_2 \cdot (1-x)\text{Na}_{2/3}\text{Ni}_{1/3}\text{Mn}_{2/3}\text{O}_2$  ( $x = 0, 0.3, 0.4, 0.5$ ) are prepared by a simple solid-phase sintering method. The sodium carbonate ( $\text{NaCO}_3$ ), lithium hydroxide ( $\text{LiOH} \cdot \text{H}_2\text{O}$ ), nickel oxide ( $\text{NiO}$ ) and manganese dioxide ( $\text{MnO}_2$ ) are mechanically ground well in a certain mole ratio. Subsequently, well-mixed materials are placed in a muffle furnace, calcined at  $900^\circ\text{C}$  for 18 h and naturally cooled to room temperature. Finally, the calcined composite cathode materials are immediately transferred to the glove box to avoid deterioration in the air. Nevertheless, there will still be some alkali residue on the surface. The material is put into deionized water to form a suspension and the pH value is tested to be about 9.

### Electrochemical characterization

The composite cathode material, conductive agent (Super P) and binder (PVDF dissolved in NMP at a concentration of 5 wt%) are mixed and ground into a slurry at the ratio of 80 wt%: 10 wt%: 10 wt%. Whereafter, the slurry is evenly coated on the surface of the aluminum foil, which is used as a collector fluid here, and then dried under vacuum at  $80^\circ\text{C}$  for 12 h. The dried electrode sheets are cut into 12 mm diameter discs and assembled into CR2025 cells with a diaphragm (glassy fiber, Whatman), sodium anode, and SIBs electrolyte ( $\text{NaClO}_4$ , purchased from Suzhou Duoduo). Among them, the loading amount of active material is 2–3 mg in the 12 mm diameter discs, and the injection amount of electrolyte is  $\approx 60\text{--}80 \mu\text{L}$ . Battery assembly is operated in the glove box where the water content is less than 0.5 ppm and the oxygen content is less than 1.0 ppm.

The CR2025 cells are placed in an electrochemical tester (Wuhan LAND, CT-2001A) and tested for constant current charge and discharge under certain operating conditions. Galvanostatic intermittent titration test (GITT) is used to analyze sodium ion dynamics, where the current pulse time is 20 min and resting relaxation time is 120 min. Cyclic voltammetry (CV) tests are carried out at a scan rate of  $0.1 \text{ mV s}^{-1}$  between 2.0 and 4.5 V (vs.  $\text{Na}^+/\text{Na}$ ). Electrochemical impedance spectroscopy (EIS) is performed on an electrochemical workstation (VMP2, Princeton Applied Research VersaSTAT3), and the frequency range of EIS is 100 kHz–5 mHz and the AC voltage is 10 mV.

### Material characterization

X-ray diffraction (XRD, Rigaku Smart Lab) is used to determine the crystal structure information with step size of  $0.02^\circ$  and a scan rate of  $2^\circ/\text{min}$  in the range of  $10^\circ\text{--}80^\circ$ , operating at 40 kV and 150 mA with a  $\text{Cu } K\alpha_{1/2}$  ( $\lambda = 1.5406 \text{ \AA}$ ) radiation source and graphite monochromator. Field emission scanning electron microscope (FESEM, Zeiss SUPRATM55) with an accelerating voltage of 10 kV is used to characterize the apparent morphology and equipped with the energy dispersive X-ray spectroscopy (EDS) to detect the elemental distribution. Selected area electron diffraction (SAED, FEI Tecnai F30) is used to detect information on the superlattice of the material. High-resolution transmission electron microscopy (HRTEM, JEOL-JEM 2100) is used for in-depth crystal structure analysis. Electronic state information of the elements on the surface of the material is acquired by the X-ray photoelectron spectroscopy (XPS) (Shimadzu Kratos Axis Ultra DLD), which is excited by  $K\alpha$  rays (1486.7 eV) from the Al target. The more structural features are expressed in the Raman spectrum fitted with a solid-state laser and a wavelength of 532 nm.

To test the material in different charge and discharge states, the positive electrode sheet is removed from the cell, placed in a glove box filled with argon atmosphere, and washed in dimethyl carbonate (DMC) to remove the remaining electrolyte. For a series of ex-situ tests, the material is transported in a vacuum bag. Opening the container is prohibited until the material is ready to be tested.

### Acknowledgements

This work is financially supported by the National Natural Science Foundation of China (Grants 51972023).

### Conflict of Interest

The authors declare no conflict of interest.

### Data Availability Statement

Research data are not shared.

**Keywords:** composite cathode material • P2-O2 phase transition • sodium-ion battery • structural stability • superlattice

- [1] C. Delmas, *Adv. Energy Mater.* **2018**, *8*, 1703137.
- [2] Y. Xu, Z. Guo, J. Wang, Z. Chen, J. Yin, Z. Zhang, J. Huang, J. Qian, X. Wang, *ACS Appl. Mater. Interfaces* **2021**, *13*, 27129–27139.
- [3] X. Shi, Q. Wang, S. Yang, Y. Qian, *ACS Sustainable Chem. Eng.* **2021**, *9*, 4583–4599.
- [4] J. W. Lund, D. H. Freestod, T. L. Boyd, *Geothermics* **2011**, *40*, 159–180.
- [5] G. Zhu, Y. Su, P. Bai, J. Chen, Q. Jing, W. Yang, Z. L. Wang, *ACS Nano* **2014**, *8*, 6031–6037.
- [6] Y. C. Lyu, Y. C. Liu, Z.-E. Yu, N. Su, Y. Liu, W. Li, Q. Li, B. Guo, B. Liu, *Sustain. Mater. Techno.* **2019**, *21*, 00098.
- [7] J.-Y. Hwang, S.-T. Myung, Y.-K. Sun, *Chem. Soc. Rev.* **2017**, *46*, 3529–3614.
- [8] a) X. Han, M. Ouyang, L. Lu, J. Li, Y. Zheng, Z. Li, *J. Power Sources* **2014**, *251*, 38–54; b) A. Masias, J. Marcicki, W. A. Paxton, *ACS Energy Lett.* **2021**, *6*, 621–630.

- [9] X.-J. Nie, X.-T. Xi, Y. Yang, Q.-L. Ning, J.-Z. Guo, M.-Y. Wang, Z.-Y. Gu, X.-L. Wu, *Electrochim. Acta* **2019**, *320*, 134626.
- [10] a) N. Yabuuchi, K. Kubota, M. Dahbi, S. Komaba, *Chem. Rev.* **2014**, *114*, 11636–11682; b) K. Chayambuka, G. Mulder, D. L. Danilov, P. H. Notten, *Adv. Energy Mater.* **2018**, *8*, 1800079; c) M. Chen, Q. Liu, S. W. Wang, E. Wang, X. Guo, S. L. Chou, *Adv. Energy Mater.* **2019**, *9*, 1803609.
- [11] a) X.-H. Ma, L.-L. Li, L. Cheng, F. Qiao, Y.-Y. Ye, N. Li, M.-L. Sha, Z.-F. Zi, J.-M. Dai, *J. Alloys Compd.* **2020**, *815*, 152402; b) S.-Y. Xu, X.-Y. Wu, Y.-M. Li, Y.-S. Hu, L.-Q. Chen, *Chinese Phys. B* **2014**, *23*, 118202; c) Y.-J. Guo, P.-F. Wang, Y.-B. Niu, X.-D. Zhang, Q. Li, X. Yu, M. Fan, W.-P. Chen, Y. Yu, X. Liu, *Nat. Commun.* **2021**, *12*, 1–11.
- [12] a) L. Deng, G. Sun, K. Goh, L.-L. Zheng, F.-D. Yu, X.-L. Sui, L. Zhao, Z.-B. Wang, *Electrochim. Acta* **2019**, *298*, 459–467; b) Y. Jiang, X. Zhou, D. Li, X. Cheng, F. Liu, Y. Yu, *Adv. Energy Mater.* **2018**, *8*, 1800068.
- [13] J. Qian, D. Ma, Z. Xu, D. Li, J. Wang, *Sol. Energy Mater. Sol. Cells* **2018**, *177*, 9–14.
- [14] E. Zhang, B. Wang, X. Yu, J. Zhu, L. Wang, B. Lu, *Energy Storage Mater.* **2017**, *8*, 147–152.
- [15] a) S. Komaba, N. Yabuuchi, T. Nakayama, A. Ogata, T. Ishikawa, I. Nakai, *Inorg. Chem.* **2012**, *51*, 6211–6220; b) M. Leng, J. Bi, W. Wang, Z. Xing, W. Yan, X. Gao, J. Wang, R. Liu, *J. Alloys Compd.* **2020**, *816*, 152581; c) L. Mu, S. Xu, Y. Li, Y. S. Hu, H. Li, L. Chen, X. Huang, *Adv. Mater.* **2015**, *27*, 6928–6933; d) J. H. Jo, J. U. Choi, A. Konarov, H. Yashiro, S. Yuan, L. Shi, Y. K. Sun, S. T. Myung, *Adv. Funct. Mater.* **2018**, *28*, 1705968.
- [16] a) J. Zhang, W. Wang, W. Wang, S. Wang, B. Li, *ACS Appl. Mater. Interfaces* **2019**, *11*, 22051–22066; b) R. Usiskin, Y. Lu, J. Popovic, M. Law, P. Balaya, Y.-S. Hu, J. Maier, *Nat. Rev. Mater.* **2021**, *6*, 1020–1035.
- [17] a) G. Gao, D. Tie, H. Ma, H. Yu, S. Shi, B. Wang, S. Xu, L. Wang, Y. Zhao, *J. Mater. Chem. A* **2018**, *6*, 6675–6684; b) M. A. Khan, D. Han, G. Lee, Y.-I. Kim, Y.-M. Kang, *J. Alloys Compd.* **2019**, *771*, 987–993.
- [18] Z. Liu, R. Tian, M. Mushtaq, W. Guo, M. Yao, J. Feng, *J. Alloys Compd.* **2019**, *791*, 39–44.
- [19] X. Wang, C. Wang, K. Han, C. Niu, J. Meng, P. Hu, X. Xu, Z. Wang, Q. Li, C. Han, *Adv. Energy Mater.* **2018**, *8*, 1802180.
- [20] Z. Lu, J. Dahn, *J. Electrochem. Soc.* **2001**, *148*, A1225.
- [21] T. E. Mabokela, A. C. Nwanya, M. M. Ndipungwi, S. Kaba, P. Ekwere, S. T. Werry, C. O. Ikpo, K. D. Modibane, E. I. Iwuoha, *J. Electrochem. Soc.* **2021**, *168*, 070530.
- [22] a) J. Ge, L. Fan, A. Rao, J. Zhou, B. Lu, *Nat. Sustain.* **2022**, *5*, 225–234; b) M. Tang, Y. Wu, Y. Chen, C. Jiang, S. Zhu, S. Zhuo, C. Wang, *J. Mater. Chem. A* **2019**, *7*, 486–492; c) L. Fan, Y. Hu, A. M. Rao, J. Zhou, Z. Hou, C. Wang, B. Lu, *Small Methods* **2021**, *5*, 2101131.
- [23] a) C. Wang, L. Liu, S. Zhao, Y. Liu, Y. Yang, H. Yu, S. Lee, G.-H. Lee, Y.-M. Kang, R. Liu, F. Li, J. Chen, *Nat. Commun.* **2021**, *12*, 2256; b) P.-F. Wang, Y. Xiao, N. Piao, Q.-C. Wang, X. Ji, T. Jin, Y.-J. Guo, S. Liu, T. Deng, C. Cui, L. Chen, Y.-G. Guo, X.-Q. Yang, C. Wang, *Nano Energy* **2020**, *69*, 104474.
- [24] Q. Shen, Y. Liu, X. Zhao, J. Jin, Y. Wang, S. Li, P. Li, X. Qu, L. Jiao, *Adv. Funct. Mater.* **2021**, *31*, 2106923.
- [25] P. K. Nayak, J. Grinblat, M. Levi, E. Levi, S. Kim, J. W. Choi, D. Aurbach, *Adv. Energy Mater.* **2016**, *6*, 1502398.
- [26] Y. Hu, Y. Gao, L. Fan, Y. Zhang, B. Wang, Z. Qin, J. Zhou, B. Lu, *Adv. Energy Mater.* **2020**, *10*, 2070198.
- [27] A. Mahmood, S. Li, Z. Ali, H. Tabassum, B. Zhu, Z. Liang, W. Meng, W. Aftab, W. Guo, H. Zhang, M. Yousaf, S. Gao, R. Zou, Y. Zhao, *Adv. Mater.* **2019**, *31*, 1805430.

Manuscript received: March 10, 2022

Revised manuscript received: April 3, 2022

Accepted manuscript online: April 5, 2022

Version of record online: April 25, 2022